

## Identifiability of Ludwik's law parameters depending on the sample geometry via inverse identification procedure

Andrija Zaplatic<sup>1a</sup>, Zvonimir Tomičević<sup>\*1</sup>, Damjan Čakmak<sup>1b</sup> and François Hild<sup>2c</sup>

<sup>1</sup>Faculty of Mechanical Engineering and Naval Architecture, University of Zagreb,  
Ivana Lučića 5, 10002 Zagreb, Croatia

<sup>2</sup>Univervisity Paris-Saclay, CentraleSupélec, ENS Paris-Saclay, CNRS, LMPS-Laboratoire de Mécanique  
Paris-Saclay, 91190 Gif-sur-Yvette, France

(Received July 30, 2021, Revised November 21, 2021, Accepted November 22, 2021)

**Abstract.** The accurate prediction of elastoplasticity under prescribed workloads is essential in the optimization of engineering structures. Mechanical experiments are carried out with the goal of obtaining reliable sets of material parameters for a chosen constitutive law via inverse identification. In this work, two sample geometries made of high strength steel plates were evaluated to determine the optimal configuration for the identification of Ludwik's nonlinear isotropic hardening law. Finite element model updating (FEMU) was used to calibrate the material parameters. FEMU computes the parameter changes based on the Hessian matrix, and the sensitivity fields that report changes of computed fields with respect to material parameter changes. A sensitivity analysis was performed to determine the influence of the sample geometry on parameter identifiability. It was concluded that the sample with thinned gauge region with a large curvature radius provided more reliable material parameters.

**Keywords:** full-field measurements; HARDOX 450; inverse identification; sample geometry; sensitivity analysis

### 1. Introduction

The development of advanced high strength materials requires optimization procedures of engineering structures and components. The optimization is carried using numerical tools, e.g., finite element (FE) simulations (Tisza 2005). To run reliable numerical simulations, trustworthy material properties are needed. Therefore, mechanical tests are conducted to determine material parameters.

Classical measuring devices (e.g., mechanical extensometer, load cells) provide only global data. The drawback of the latter ones is that local effects cannot be captured. The development of digital imaging and full-field measurement methods provide means to capture localized phenomena. Digital Image Correlation or DIC (Sutton *et al.* 2009) stands out nowadays as the most versatile and most widely used measurement technique in experimental mechanics. The application of DIC is

---

\*Corresponding author, Assistant Professor, E-mail: zvonimir.tomicevic@fsb.hr

<sup>a</sup>Ph.D. Student, E-mail: andrija.zaplatic@fsb.hr

<sup>b</sup>Ph.D., E-mail: damjan.cakmak@fsb.hr

<sup>c</sup>Research Professor, E-mail: francois.hild@ens-paris-saclay.fr

straightforward as digital images are used as the source of information, i.e., capturing the motions of monitored surfaces. Besnard *et al.* (2006) developed FE-based DIC where FE meshes were utilized to discretize the observed region of interest, and the output were measured nodal displacements. Such approach is powerful since experimental data and numerical simulations can be directly coupled in inverse identification schemes (Lecompte *et al.* 2007, Cooreman *et al.* 2008).

Finite Element Model Updating or FEMU (Kavanagh and Clough 1971) is a well-known identification procedure, which was considered in the present work. FEMU is an iterative scheme that minimizes the differences between experimentally measured and numerically computed quantities (Prates *et al.* 2016, Martins *et al.* 2018), e.g., measured and calculated displacement fields, and measured load and calculated global reaction forces on the FE model. FEMU is one of the most versatile identification procedures as it can be employed for, say, uniaxial (Tomičević *et al.* 2016a) and biaxial (Tomičević *et al.* 2016b) tests. Furthermore, FEMU is not limited to macroscopic laws. Guery *et al.* (2016) used the same framework to calibrate crystal plasticity parameters of AISI 316LN stainless steel. Compared to other inverse identification methods (e.g., Virtual Fields Method (Grediac and Pierron 2006), Constitutive Equation Gap Method (Geymonat *et al.* 2002) and the Equilibrium Gap Method (Claire *et al.* 2004)), FEMU was proven to provide the most accurate results in the presence of data corrupted with acquisition noise (Martins *et al.* 2018, Roux *et al.* 2020). FEMU is a sensitivity-based identification method (Tarantola 1987), i.e., the influence of material parameter changes on observed quantities is evaluated. Therefore, FEMU was also used for sample optimization to tailor the geometry to activate specific material parameters. Bertin *et al.* (2016) used the aforementioned procedure to optimize the fillet radii of a cruciform specimen for biaxial testing. Furthermore, FEMU was then used to calibrate material parameters of the Hill-1948 plasticity model with a *single* biaxial test (Bertin *et al.* 2017).

The aim of this paper is to evaluate two distinct sample geometries used in tensile tests for parameter identification. The samples were made from high strength steel plates. The goal was to determine the best of the two geometries for calibrating Ludwik's nonlinear isotropic hardening law. FEMU was deemed a suitable choice for the sensitivity analysis. Using FEMU, sensitivity fields (Negggers *et al.* 2017, Ahmed *et al.* 2019, Prates *et al.* 2019) and the Hessian matrices (Bertin *et al.* 2016) were extracted to evaluate the parameter sensitivity with respect to the sample geometry.

## 2. Experimental investigation

Within this research, the experimental investigation was carried out on 2 mm thick samples made of HARDOX 450 steel. Two distinct sample geometries were considered for the mechanical tests. The *DIN* sample (Fig. 1(a)) was designed with two parallel edges located in the entire gauge region. Near the ends, the sample was widened to ensure larger gripping surfaces and to disable any sample slip. Furthermore, the design induced two regions with increased stress concentrations. The second *dogbone* sample (Fig. 1(b)) was thinned in the center of the gauge area with a radius of 75 mm, thus ensuring a unique region where strain localization may occur. Two mechanical tests were carried out on a uniaxial testing machine (*Messphysik Beta 50-5*, Fig. 2(T)). The samples were subjected to uniaxial and monotonic tensile loadings under displacement control with a prescribed rate of 1 mm/min.

The surfaces of the samples were monitored by a single CCD *Dalsa Falcon* camera (Fig. 2(C)) with a definition of  $2358 \times 1728$  pixels and an image acquisition rate of 1 fps. Two light sources (Fig. 2(L)) were used to ensure uniform sample illumination. The hardware parameters of the optical setup are listed in Table 1.

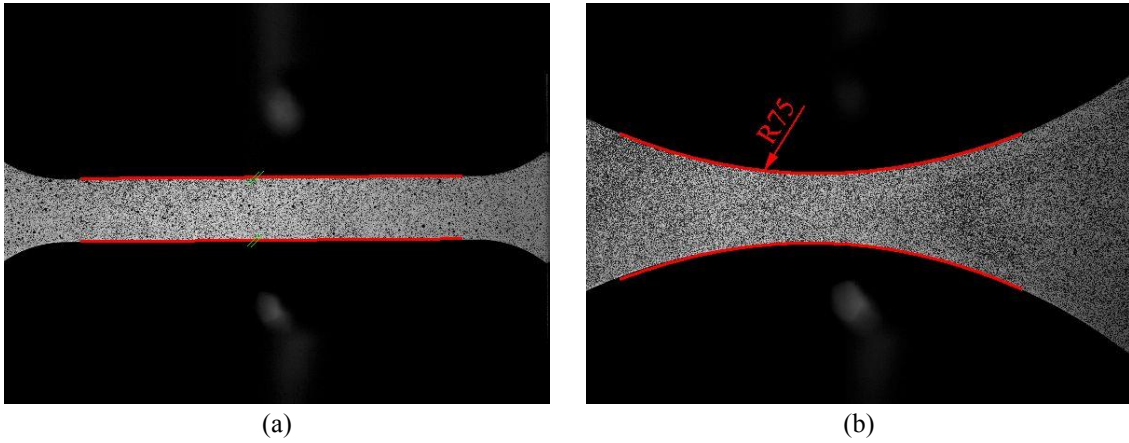


Fig. 1 Considered geometries. (a) *DIN* and (b) *dogbone* samples with specific geometric characteristics highlighted with red lines

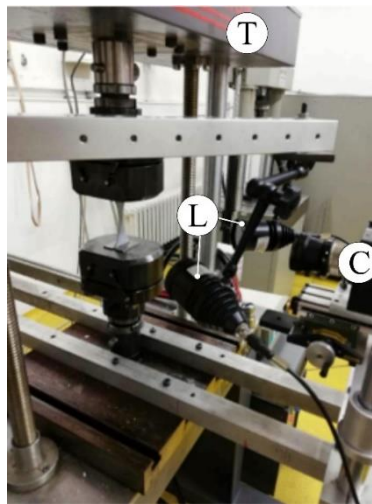


Fig. 2 Experimental setup consisting of two light sources and a single digital camera. See text for the description of the labels

Table 1 Hardware parameters of the optical setup

Camera	<i>Dalsa Falcon 4M60</i>
Definition	2358×1728 pixels (B/W images)
Color filter	None
Digitization	8 bits
Lens	Titanar 50 mm
Aperture	f/2.8
Field of view	44.4 cm <sup>2</sup>
Stand-off distance	30 cm
Image acquisition rate	1 fps
Patterning technique	B/W paints
Pattern feature size	15 px

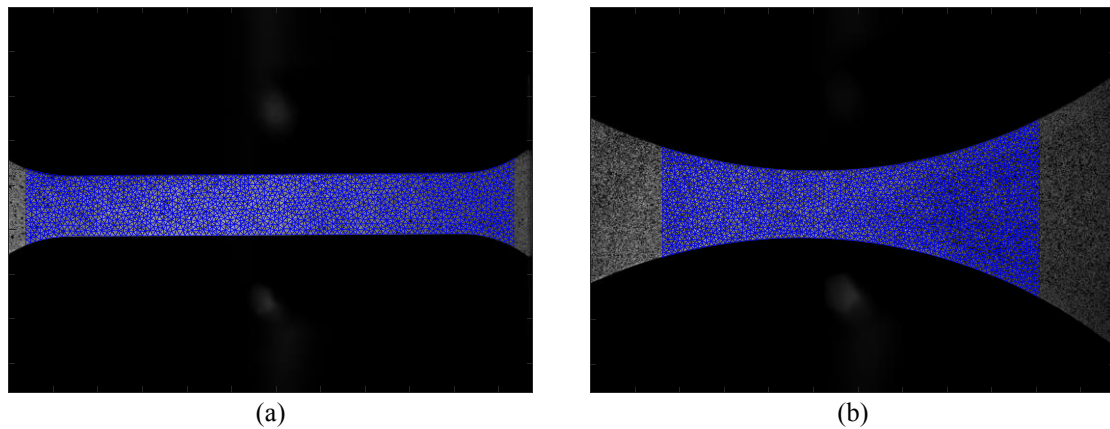


Fig. 3 Three noded finite element meshes used in the DIC procedure for (a) *DIN* and (b) *dogbone* sample

### 2.1 Full-field measurement results

For this study, Finite element (FE) based DIC was employed to measure displacement fields on the observed Region of Interest (ROI). The correlation framework *Correli 3.0*. (Leclerc *et al.* 2015) was used. The ROI was discretized with 3-noded triangular (T3) elements (Fig. 3). Furthermore, mechanical regularization (Tomičević *et al.* 2013) was implemented within the algorithm. The full analysis parameters are reported in Table 2.

Before each experiment, 10 images were acquired in the unloaded state to obtain the noise floor estimates by calculating the standard deviations of the nodal displacements and strains. For the *DIN* sample, the displacement noise floor was slightly lower than for the *dogbone* sample. On the other hand, the strain noise floor was lower for the *dogbone* sample. However, both displacement and strain noise floors were of the same order of magnitude.

Table 2 DIC analysis parameters

DIC software	Correli 3.0	
Image filtering	None	
Average element length	20 pixels	
Shape functions	Linear (T3 elements)	
Matching criterion	Penalized sum of squared differences	
Regularization length	Bulk	Edge
	100 pixels	200 pixels
Displacement noise floor	<i>DIN</i>	<i>Dogbone</i>
	0.6 $\mu\text{m}$	0.7 $\mu\text{m}$
Strain noise floor	$2 \times 10^{-4}$	$10^{-4}$

The analysis of the calculated Green-Lagrange strain fields revealed two strained bands forming an X. A single dominant band developed fully until failure for both cases (Fig. 4). Strain localization occurred in different regions. For the *DIN* sample, the strains localized on the left side near the

widening area close to the grips. For the *dogbone* sample, strain localization developed in the ligament, as expected from its geometry. A first advantage of *dogbone* samples is that they allow for a direct control of the location of the strained zone. With the *DIN* sample, localization may occur near each end of the sample. Therefore, to monitor both possible concentration zones, a larger ROI needs to be considered. Conversely, since for the *dogbone* sample the location is known in advance, the optical setup can be put closer to the sample to capture strain localization in greater details. Moreover, multi-scale DIC (Passieux *et al.* 2015) can also be employed since the strained band location is known a priori.

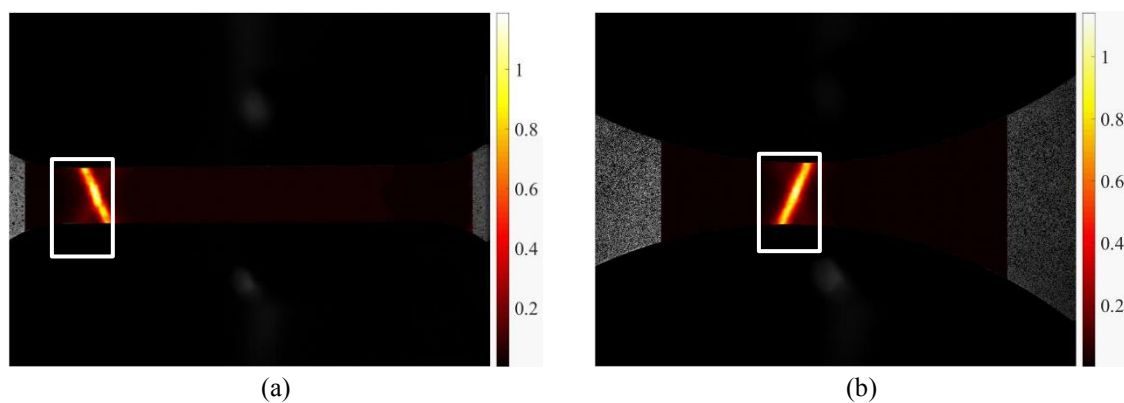


Fig. 4 Major principal strain fields for the last image captured before fracture for the *DIN* (a) and *dogbone* (b) samples. The white boxes denote the virtual strain gauge used to calculate average strain levels

The macroscopic stress-strain curves of both experiments are reported in Fig. 5. The engineering stress was calculated by dividing the measured force by the initial cross-sectional area. The Green-Lagrange strain levels were obtained by using virtual strain gauges (Fig. 4) positioned over the captured strain localization zones. In the virtual gauge, the nodal strains within the gauge were averaged for each temporal registration.

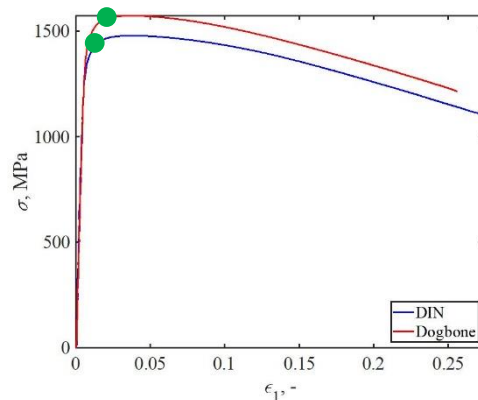


Fig. 5 Macroscopic engineering stress vs. Green Lagrange strain curves. The green circles denote the ultimate stresses where the numerical analyses were stopped

The *dogbone* sample displayed slightly prolonged elasticity (i.e., higher yield stress) than the *DIN* sample. However, for the *DIN* sample, 2% larger strains at failure were achieved (the *dogbone* sample fractured earlier due to increased strains in the localization band (Nam Do *et al.* 2015)). Moreover, a higher ultimate tensile strength was reached with the *dogbone* sample. Beyond the stress peak, material softening was very similar in both tests, which is confirmed by the strain field patterns shown in Fig. 4.

### 3. Finite element model updating

The goal of FEMU is to iteratively minimize differences between experimentally measured and numerically calculated quantities. The minimization framework iteratively updates the desired material parameters by calculating Hessian matrices that are based on sensitivity fields (Tarantola, 1987). In the present analyses, measured and calculated displacement fields were considered, as well as measured forces and global reaction forces extracted from the FE model. The employed FE meshes (Fig. 6) were prepared for the identification scheme by prescribing measured nodal displacements as Dirichlet boundary conditions on the stressed edges of the model (outlined by red lines in Fig. 6).

The FEMU mesh was constructed from the DIC mesh. The T3 mesh was converted into four-noded quadrilateral elements (Q4). Lindner *et al.* (2015) reported that 3D meshes were necessary to accurately evaluate stress states in plasticity. Therefore, the Q4 mesh was extruded to obtain a 3D mesh made of C3D8R elements with reduced integration.

In the minimization procedure, the cost function considering measured displacements is formulated as the *weighted* squared difference between the measured  $\mathbf{u}_m$  and calculated  $\mathbf{u}_c$  nodal displacements

$$\chi_u^2 \{\mathbf{p}\} = \frac{1}{N_u} (\{\mathbf{u}_m\} - \{\mathbf{u}_c\})' [\mathbf{C}_u]^{-1} (\{\mathbf{u}_m\} - \{\mathbf{u}_c\}), \quad (1)$$

where  $\{\mathbf{p}\}$  is the vector column gathering all the sought material parameters,  $[\mathbf{C}_u]$  the covariance matrix equal to  $2\gamma_f^2[\mathbf{M}]^{-1}$ ,  $[\mathbf{M}]$  the global DIC matrix (Hild and Roux 2012),  $\gamma_f^2$  the variance of

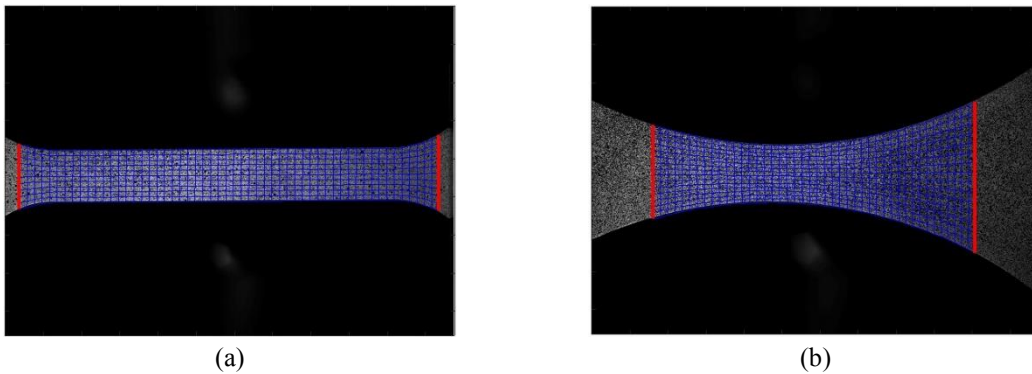


Fig. 6 Finite element meshes used in the identification procedure for the *DIN* (a) and *dogbone* samples. The red lines depict areas where measured nodal displacements were defined as Dirichlet boundary conditions

Gaussian white noise associated with image acquisition, and  $N_u$  the number of kinematic degrees of freedom (Mathieu *et al.* 2015).

The cost function considering measured load and extracted reaction forces from the stressed edges of the FE mesh are expressed as

$$\chi_F^2 \{\mathbf{p}\} = \frac{1}{\gamma_F^2 \cdot N_F} \|\{\mathbf{F}_m\} - \{\mathbf{F}_c\}\|^2, \quad (2)$$

where  $\gamma_F$  is the standard uncertainty of the load cell, and  $N_F$  the number of load data.

By introducing a weight  $\omega$ , the two previous cost functions are combined as

$$\chi_{\text{tot}}^2 \{\mathbf{p}\} = (1 - \omega) \chi_u^2 + \omega \chi_F^2, \quad (3)$$

For the present study,  $\omega$  was set to 0.5 to provide equal weight to kinematic and static data.

The minimization of the kinematic cost function was carried out thanks to the evaluation of kinematic sensitivity fields. The computed displacement vector, for any iteration  $i$ , is Taylor expanded as

$$\mathbf{u}_c(\mathbf{x}, t, \{\mathbf{p}^{(i)}\}) = \mathbf{u}_c(\mathbf{x}, t, \{\mathbf{p}^{(i-1)}\}) + \frac{\partial \mathbf{u}_c}{\partial \{\mathbf{p}\}}(\mathbf{x}, t, \{\mathbf{p}^{(i-1)}\}) \{\partial \mathbf{p}\}, \quad (4)$$

where  $\{\partial \mathbf{p}\}$  is the increment to the sought parameters, and from Eq. (4), the displacement sensitivity matrix becomes

$$[\mathbf{S}_u] = \frac{\partial \mathbf{u}_c}{\partial \{\mathbf{p}\}}. \quad (5)$$

The displacement sensitivity matrix accounts for changes in displacement fields due to a small variation of each sought material parameter, and is updated for each iteration. The parameter increment is then expressed as a function of the sensitivity matrix

$$\{\partial \mathbf{p}\} = \frac{1}{2\gamma_f^2} [\mathbf{H}_u^{(i-1)}]^{-1} [\mathbf{S}_u^{(i-1)}]^t [\mathbf{M}] (\{\mathbf{u}_m\} - \{\mathbf{u}_c^{(i-1)}\}), \quad (6)$$

where  $[\mathbf{H}_u^{(i-1)}]$  is the Hessian matrix expressed as a function of the sensitivity matrix

$$[\mathbf{H}_u^{(i-1)}] = \frac{1}{2\gamma_f^2} [\mathbf{S}_u^{(i-1)}]^t [\mathbf{M}] [\mathbf{S}_u^{(i-1)}]. \quad (7)$$

The parameter increment considering only measured loads and computed global reaction forces reads

$$\{\partial \mathbf{p}\} = \left( \left( [\mathbf{S}_F]^{(i-1)} \right)^t [\mathbf{S}_F]^{(i-1)} \right)^{-1} [\mathbf{S}_F]^{(i-1)} \{\mathbf{F}_m - \mathbf{F}_c^{(i-1)}\}. \quad (8)$$

where  $[\mathbf{S}_F]$  denotes the force sensitivity matrix. The Hessian matrix considering force data is expressed as

$$[\mathbf{H}_F] = \frac{1}{\gamma_F^2} [\mathbf{S}_F]^t [\mathbf{S}_F]. \quad (9)$$

For the proposed FEMU-UF (Mathieu *et al.* 2015, Tomičević *et al.* 2016) approach, the global Hessian matrix  $[\mathbf{H}_{\text{UF}}]$  then becomes the sum of the kinematic and static Hessian matrices

$$[\mathbf{H}_{\text{UF}}] = [\mathbf{H}_{\text{U}}] + [\mathbf{H}_{\text{F}}]. \quad (10)$$

In the following, the total Hessian matrix  $[\mathbf{H}_{\text{UF}}]$ , displacement and force sensitivity fields are evaluated and compared for both considered sample geometries.

### 3.1 Identification results

The identification procedure was carried out for both samples *independently*. The FE analyses were carried out until the ultimate strength was reached, i.e., before strain softening. For the *DIN* sample, the analyses were performed until the strain levels reached 4% (i.e., time step 435) and for the *dogbone* geometry up to 3.2% (i.e., time step 220), see Fig. 5. In the FE simulations, plasticity was described with Ludwik's isotropic hardening law (Ludwik 1909)

$$\sigma_{\text{eq}} = \sigma_y + K \varepsilon_{\text{pl}}^{-n}, \quad (11)$$

where  $\sigma_{\text{eq}}$  corresponds to von Mises' equivalent stress, and  $\varepsilon_{\text{pl}}$  the cumulated plastic strain. The sought material parameters were the Young's modulus  $E$ , yield stress  $\sigma_y$ , hardening modulus  $K$  and hardening exponent  $n$ . The Poisson's ratio was not considered and was kept constant at 0.3 since it was difficult to calibrate (Tomičević *et al.* 2016a). However, the sensitivity of the latter to sample geometry was evaluated.

For both samples, the initial parameters were identical. After the FEMU-UF procedure was run, it was observed that the sample geometry led to significant differences in calibrated parameters (Table 3). For both samples, the Young's modulus increased; for the *dogbone* geometry the value increased more. Moreover, for the latter, the calibrated values of the yield stress  $\sigma_y$  and hardening exponent  $n$  were higher than for the *DIN* sample. For both samples, the hardening modulus  $K$  increased; for the *DIN* sample it increased more. Lower identification residuals were achieved for the *dogbone* sample.

Table 3 Calibrated material parameters for the studied geometries

	$E$ , GPa	$\sigma_y$ , MPa	$K$ , MPa	$n$ , -	$\chi_{\text{total}}$
Initial	210	1200	700	0.2	-
<i>DIN</i>	211	1060	980	0.18	41.3
<i>Dogbone</i>	219	1150	920	0.19	33.3

The identification procedure led to parameters that provided a good description of the nonlinear behavior for both samples. In Fig. 7, the global reaction forces are displayed for the initial and calibrated material parameters. For the *DIN* sample, the onset of plasticity was not described as accurately, which led to increased global FEMU-UF residuals (i.e.,  $\chi_{\text{total}}$ ). Conversely, for the *dogbone* geometry lower deviations from the *Reference* curve were observed for the reaction force with the calibrated parameters.

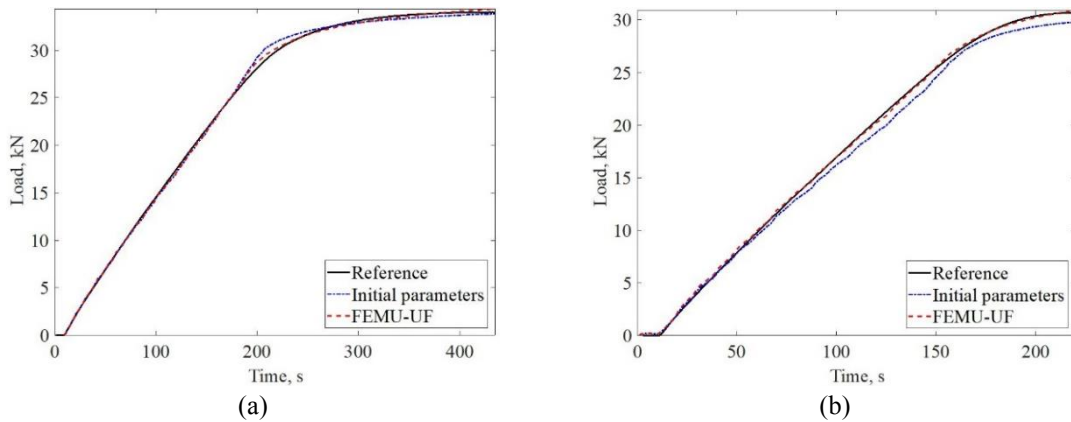


Fig. 7 Comparison of measured load (Reference) and reaction forces extracted from the FE model for the initial and calibrated elastoplastic parameters via FEMU-UF. (a) *DIN* and (b) *dogbone* samples

#### 4. Sensitivity analysis

The parameter sensitivity for the two considered sample geometries (i.e., *DIN* and *dogbone*) was evaluated with the Hessian matrices calculated within the FEMU framework. The Hessian matrix is of size  $n \times n$ , where  $n$  corresponds to the number of sought parameters. Furthermore, the Hessian matrix gathers displacement *and* force sensitivities to parameter changes. The diagonal terms in the Hessian matrices describe the parameter sensitivities when considered independently, whereas the off-diagonal terms report on correlative influences of parameters. The evaluation of the Hessian matrix was performed prior to the identification procedure to determine the optimal strategy for material parameter calibration.

The Hessian matrices are shown in Fig. 8. For the *DIN* sample, twice as much images were captured and analyzed (i.e., 435 images) compared to the *dogbone* sample (i.e., 220 images). Therefore, a first order approximation was carried out on the *DIN* Hessian so it could be compared to the *dogbone* Hessian. First, all members of the *DIN* Hessian matrix were divided by the number of images (i.e., 435) and then multiplied by the number of images captured for the *dogbone* sample.

It is observed that for the Young's  $E$ , the highest sensitivity is achieved by the *dogbone* geometry. This result also applies for the Poisson's ratio  $\nu$  and hardening exponent  $n$ . The correlative influences between  $E$  and other parameters are slightly higher for the *DIN* sample. Furthermore, for the Poisson's ratio, the *dogbone* sample provided the highest sensitivity. This property can also be stated for the correlative influences, which are higher than for the *DIN* sample. The yield stress  $\sigma_y$  sensitivity is similar for both geometries, although it is slightly higher for the *DIN* sample. Opposite trends are observed for the correlative influences between  $\sigma_y$  and  $E$ . For the *DIN* sample, they are correlated, whereas for the *dogbone* sample they are anti-correlated. The hardening parameter  $K$  exhibits greater sensitivity for the *DIN* sample than for its counterpart. However, the correlative influences of other parameters on  $K$  also need to be considered, which are on average higher for the *dogbone* sample. For the latter, the sensitivity of the hardening exponent  $n$  is seven times higher than for the *DIN* sample, thus rendering it easier to calibrate.

Last, the conditioning of the two matrices was estimated from the spectrum of eigen values (Fig. 8). For the *DIN* sample, the log-condition number was equal to 3, whereas for the *dogbone* it was 4. The condition number is preferred to be as small as possible thus indicating that the eigen values

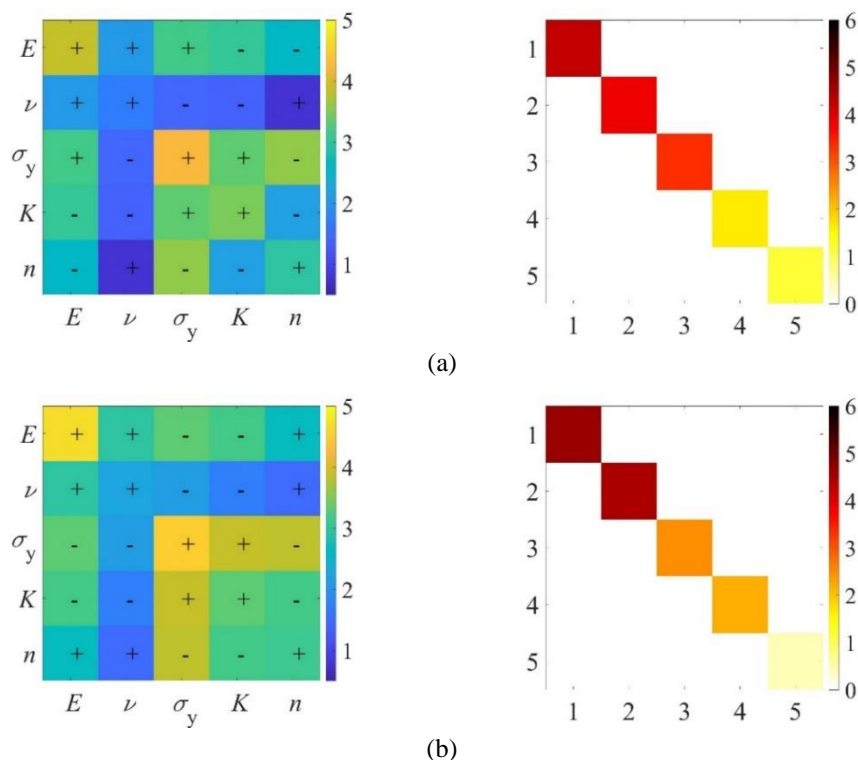


Fig. 8 Decimal logarithm of Hessian matrices  $[\mathbf{H}_{UF}]$  (first column) and corresponding diagonalized matrices (second column) for the *DIN* (a) and *dogbone* (b) geometries

for all parameters are similar, and therefore easier to calibrate. In this case, the *DIN* sample provides the smallest condition number and all eigen values are greater than 1. On the other hand, for the *dogbone* sample, the lowest eigenvalue expressed in decimal logarithm is less than 1. Furthermore, the largest eigenvalue was found for the *dogbone* sample. Moreover, the first two eigenvalues are much higher for the *dogbone* sample than for the *DIN* sample. From the presented data, it is observed that the *dogbone* sample provides the highest sensitivities (as observed from the Hessian and its eigen values). Yet, with the aforementioned sample, the lowest eigenvalue is also achieved, which is a drawback.

Figs. 9-13 display the displacement sensitivity fields  $[\mathbf{S}_u]$  for each considered material parameter and for each sample geometry. A parameter offset  $\varepsilon=1\%$  was considered. Each figure is composed of two subfigures, which are divided into four sensitivity fields. Each figure is also divided into two rows, where the first one displays sensitivities with respect to the  $x$ -axis, and the second to the  $y$ -axis. On each sensitivity field, a vertical dashed line is depicted, which corresponds to the column of pixels used to create the sensitivity history with respect to analyzed images (i.e., subfigures next to sensitivity fields). The positive  $x$ -axis is oriented to the right, whereas the positive  $y$ -axis is oriented toward the top of the page. For most parameters, the sensitivities in elasticity are small in comparison to plasticity. To calibrate the Young's modulus, elasticity is sufficient.

The Young's modulus sensitivity fields for both samples are different in terms of distribution (Fig. 9). For the *dogbone* sample, increased sensitivities occur around the strain localization zone

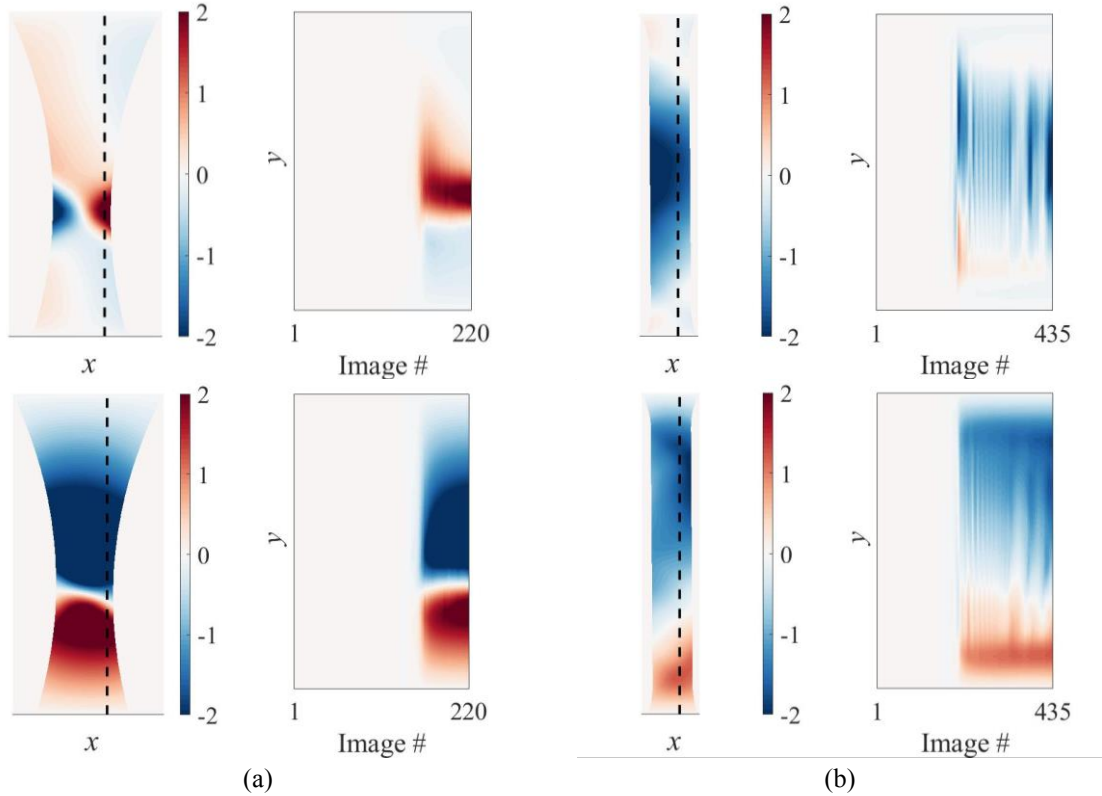


Fig. 9 Displacement sensitivity fields for  $E$  in terms of  $x$  (first row) and  $y$  (second row) displacements expressed in pixel/ $\varepsilon$ . The sensitivity fields are displayed for the last analyzed image. A line of pixels is plotted for each analyzed image next to the sensitivity field

(i.e., in plasticity). For the *DIN* sample, increased sensitivities occur in the center of the specimen, away from the localization zones. In the  $x$ -direction, the *dogbone* geometry displays more heterogeneous sensitivities. For the  $y$ -direction, the *DIN* sample also displays heterogeneous distributions. Yet, it is more uniform through the loading history for the *dogbone* sample. The *dogbone* sensitivity fields are more pronounced than for the *DIN* sample.

The Poisson's ratio displacement sensitivity fields  $[S_u]$  in the  $x$ -direction are similar for both geometries (Fig. 10). From the sensitivity history plot, it is observed that for the *dogbone* sample the sensitivity levels are slightly higher. For the  $y$ -direction, the sensitivities are smaller, thereby indicating, as expected, lower sensitivities in the loading direction. The Poisson's ratio sensitivities are the lowest compared to the other parameters.

The yield stress displacement sensitivity  $[S_u]$  is more pronounced for the *DIN* sample in both directions, whereas for the *dogbone* sample the  $y$ -direction is more noticeable (Fig. 11). The latter exhibits more uniformly distributed and higher sensitivities in the history plot than its *DIN* counterpart. Increased sensitivities are present around the strain localization zone. For the *DIN* sample, throughout the sensitivity history, nonuniform distributions are observed. Moreover, a change in sensitivity values from negative to positive occurred at both ends (i.e., areas of increased stress concentration) of the *DIN* sample in both directions.

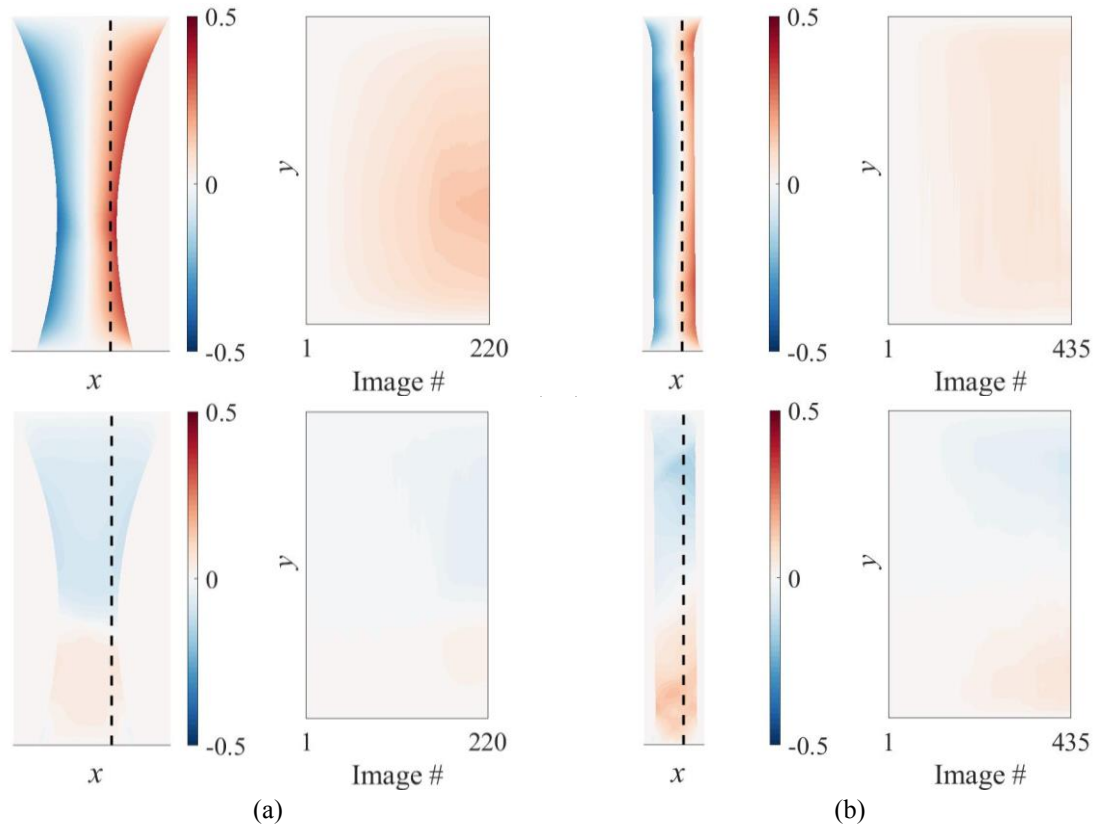


Fig. 10 Displacement sensitivity fields for  $v$  in terms of  $x$  (first row) and  $y$  (second row) displacements expressed in pixel/ $\epsilon$ . The sensitivity fields are displayed for the last analyzed image. A line of pixel values is plotted for each analyzed image next to the sensitivity field

For the hardening modulus  $K$ , the *dogbone* sample displays localized areas of increased positive sensitivities, whereas in the *DIN* sample they encompass almost the entire region of interest. However, around the reported strain band, the change from positive to negative sensitivities is observed in both  $x$ - and  $y$ -directions, as is the case for the *dogbone* sample. Moreover, for the *DIN* sample, the sensitivity fields are similar in both directions. The same observation applies for the *dogbone* sample. However, the sensitivities are more pronounced in the  $y$ -direction. As was the case in the Hessian matrix analysis, the *DIN* sample overall exhibits more pronounced sensitivities. However, it is numerically easier to describe the *dogbone* sample response as the strain localization zone is known *a priori*. Therefore, the FE algorithm can accurately predict where localization will occur. Without prescribed experimentally measured displacements, the FE algorithm may not predict the strain localization zone for the *DIN* sample.

When comparing the sensitivities for the hardening exponent  $n$  (Fig. 13), the fields for the *DIN* sample display more pronounced sensitivities. However, as previously displayed for the *dogbone* sample, the sensitivities are localized around the strain band location, whereas for the *DIN* sample most of the region of interest contains positive sensitivities. From the *DIN* sensitivity field and history, it is observed that the sensitivities are also localized around the detected strain band, near the gripped part of the sample.

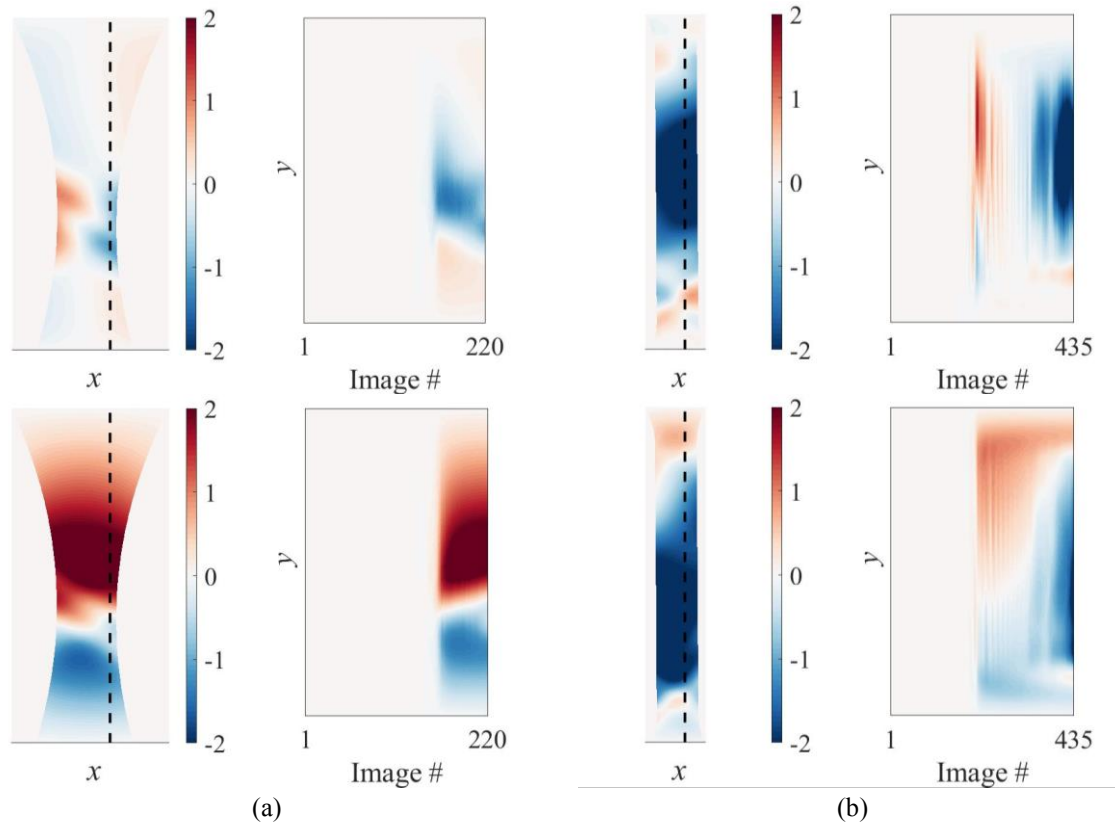


Fig. 11 Displacement sensitivity fields for  $\sigma_Y$  in terms of the  $x$  (first row) and  $y$  (second row) displacements expressed in pixel/ $\varepsilon$ . The sensitivity fields are displayed for the last analyzed image respectively. A line of pixel values is plotted for each analyzed image next to the sensitivity field

Fig. 14 displays the influence of individual parameter changes on the computed reaction forces. The force sensitivities are expressed as load [N] divided by parameter offset  $\varepsilon$ . Similar trends are observed for both samples. The sensitivity levels for the *dogbone* sample are slightly lower than for the *DIN* geometry. For both geometries, the Young's modulus  $E$  displays the highest sensitivity from all considered parameters; the highest levels are in elasticity. In plasticity,  $E$  displays reduced force sensitivities. As expected, the Poisson's ratio displays negligible influence on the force and displacement sensitivities. The yield stress leads to the second highest sensitivity. It is the only parameter that provides sensitivities of the same order of magnitude as  $E$ . Conversely, the hardening parameters display an order of magnitude lower sensitivities. When comparing  $E$  with the plastic parameters, it is observed that when  $E$  reaches the lowest sensitivity values the latter ones reach their maximum levels.

## 5. Conclusions

An experimental and numerical comparison of the two considered configurations (i.e., *DIN* and

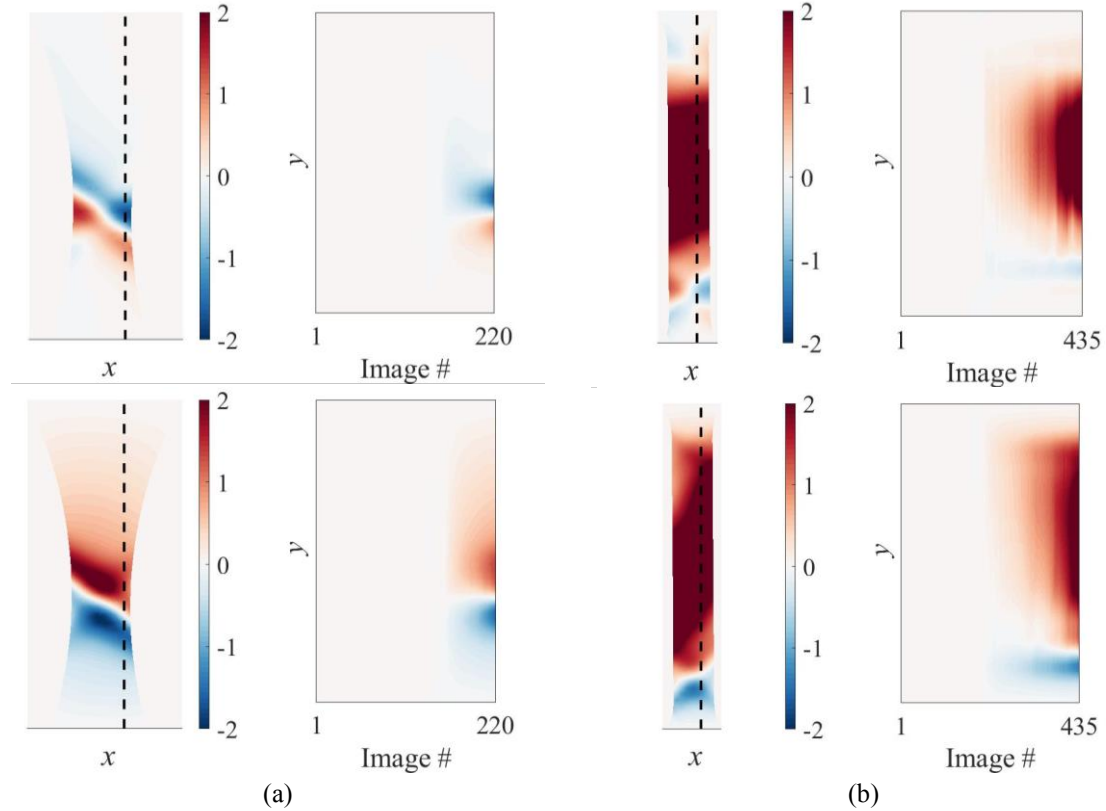


Fig. 12 Displacement sensitivity fields for  $K$  in terms of  $x$  (first row) and  $y$  (second row) displacements expressed in  $\text{pixel}/\varepsilon$ . The sensitivity fields are displayed for the last analyzed image. A line of pixels is plotted for each analyzed image next to the sensitivity field

*dogbone*) was performed to determine the sample geometry with highest parameter sensitivities in uniaxial tensile tests for the calibration of Ludwik's law parameters. The *DIN* sample contained two parallel edges in the gauge region, whereas the *dogbone* sample was thinned in the center with a radius of 75 mm. The main results of this work are:

- the *DIN* sample provided better condition number of the diagonalized Hessian matrix,
- the *dogbone* sample displayed higher sensitivity for the elastic parameters (i.e., Young's modulus  $E$  and Poisson's ratio  $\nu$ ),
- similar sensitivities were reported for the yield stress  $\sigma_y$ ,
- higher sensitivity for the hardening modulus  $K$  was observed for the *DIN* sample, whereas for the hardening exponent  $n$ , higher sensitivity was observed for its counterpart,
- the *dogbone* sample exhibited increased sensitivity to parameter changes around the strain localization zone.

Both samples exhibited advantages and drawbacks with respect to each other, especially in the identifiability of material parameters. However, due to the *a priori* known strain localization area, the *dogbone* sample is a more suitable choice since a smaller region of the sample can be monitored in more detail.

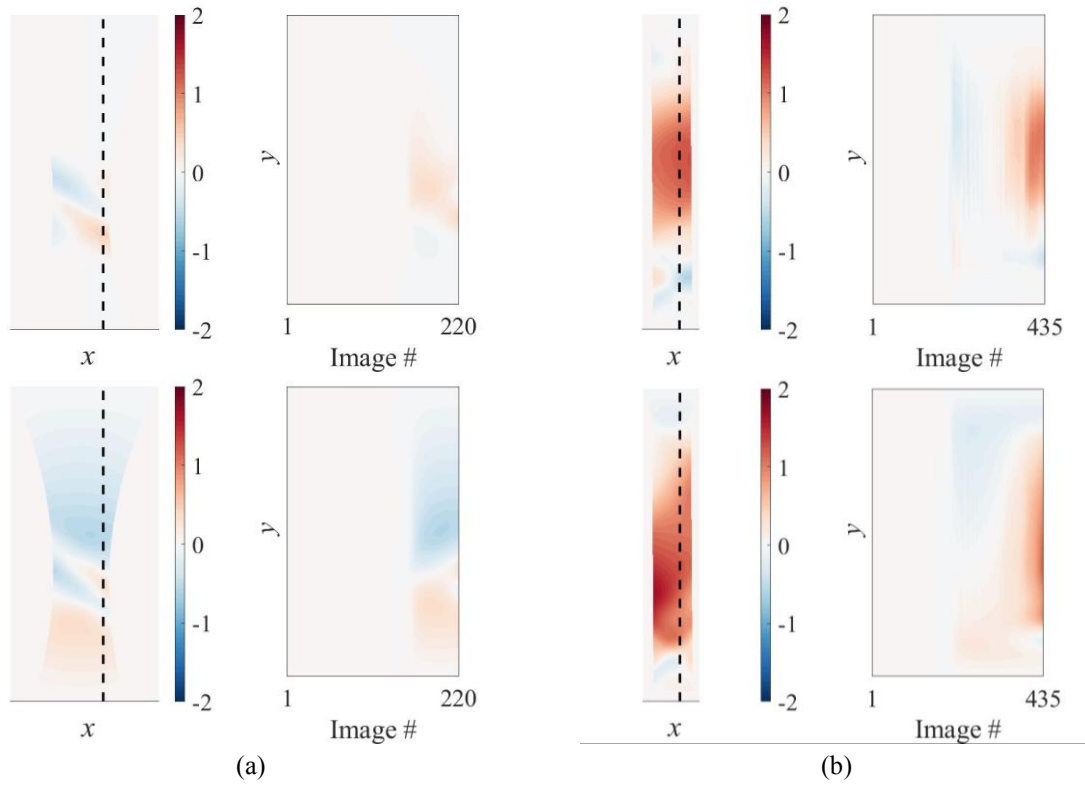


Fig. 13 Displacement sensitivity fields for  $n$  in terms of  $x$  (first row) and  $y$  (second row) displacements expressed in pixel/ $\varepsilon$ . The sensitivity fields are displayed for the last analyzed image. A line of pixels is plotted for each analyzed image next to the sensitivity field

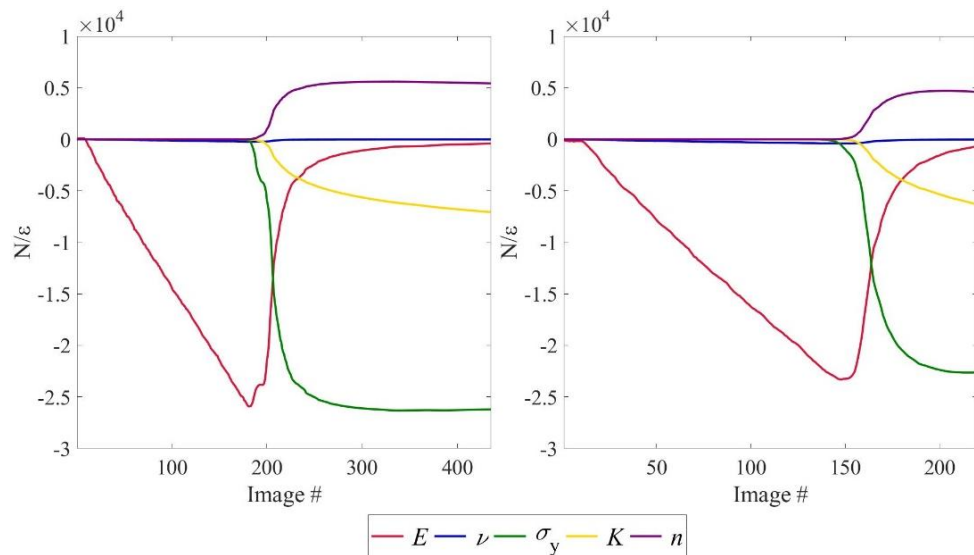


Fig. 14 Force sensitivities expressed in  $N/\varepsilon$  for the *DIN* (left) and *dogbone* (right) geometries

Last, it is worth noting that the present framework, which was applied to Ludwik's law up to the ultimate load, can be used to analyze different constitutive postulates as well as different geometries. The framework is generic and versatile provided the numerical simulations are able to capture the main experimental features of the considered experiment.

## Acknowledgments

This work was performed within the FULLINSPECT project supported by the Croatian Science Foundation (UIP-2019-04-5460 Grant).

## References

- Ahmed, S.T., Aguib, S., Toufik, T., Noureddine, C. and Ahmed, C. (2019), "Effects of the geometrical parameters of the core on the mechanical behavior of sandwich honeycomb panel", *Couple. Syst. Mech.*, **8**(6), 473-488. <https://doi.org/10.12989/csm.2019.8.6.473>.
- Bertin, M., Hild, F. and Roux, S. (2016), "Optimization of a cruciform specimen geometry for the identification of constitutive parameters based upon full-field measurements", *Strain*, **52**(4), 307-323. <https://doi.org/10.1111/str.12178>.
- Bertin, M., Hild, F. and Roux, S. (2017), "On the identifiability of Hill-1948 plasticity model with a single biaxial test on very thin sheet", *Strain*, **53**(5), e12233, <https://doi.org/10.1111/str.12233>.
- Bertin, M., Hild, F., Roux, S., Mathieu, F., Leclerc, H. and Aïmedieu, P. (2016), "Integrated digital image correlation applied to elastoplastic identification in a biaxial experiment", *J. Strain Anal. Eng. Des.*, **51**(2), 118-131. <https://doi.org/10.1177/0309324715614759>.
- Besnard, G., Hild, F. and Roux, S. (2006), "'Finite-element' displacement fields analysis from digital images: Application to Portevin-Le Châtelier bands", *Exp. Mech.*, **46**(6), 789-803. <https://doi.org/10.1007/s11340-006-9824-8>.
- Claire, D., Hild, F. and Roux, S. (2004), "A finite element formulation to identify damage fields: The equilibrium gap method", *Int. J. Numer. Meth. Eng.*, **61**(2), 189-208. <https://doi.org/10.1002/nme.1057>.
- Cooreman, S., Lecompte, D., Sol, H., Vantomme, J. and Debruyne, D. (2008), "Identification of mechanical material behavior through inverse modeling and DIC", *Conf. Proc. Soc. Exp. Mech. Ser.*, **65**(4), 421-433. <https://doi.org/10.1007/s11340-007-9094-0>.
- Geymonat, G., Hild, F. and Pagano S. (2002), "Identification of elastic parameters by displacement field measurement", *Comptes Rendus Mécanique*, **330**, 403-408. [https://doi.org/10.1016/S1631-0721\(02\)01476-6](https://doi.org/10.1016/S1631-0721(02)01476-6).
- Grediac, M. and Pierron F. (2006), "Applying the virtual fields method to the identification of elasto-plastic constitutive parameters", *Int. J. Plast.*, **22**(4), 602-627. <https://doi.org/10.1016/j.ijplas.2005.04.007>.
- Guery, A., Hild, F., Latourte, F. and Roux, S. (2016), "Identification of crystal plasticity parameters using DIC measurements and weighted FEMU", *Mech. Mater.*, **100**, 55-71. <https://doi.org/10.1016/j.mechmat.2016.06.007>.
- Hild, F. and Roux, S. (2012), "Comparison of local and global approaches to digital image correlation", *Exp. Mech.*, **52**(9), 1503-1519. <https://doi.org/10.1007/s11340-012-9603-7>.
- Kavanagh, K.T. and Clough, R.W. (1971), "Finite element applications in the characterization of elastic solids", *Int. J. Solid. Struct.*, **7**(1), 11-23. [https://doi.org/10.1016/0020-7683\(71\)90015-1](https://doi.org/10.1016/0020-7683(71)90015-1).
- Leclerc, H., Neggers, J., Mathieu, F., Hild, F. and Roux, S. (2015), Correli 3.0, Agence Pour la Protection des Programmes, Paris, France, IDDN.FR.001.520008.000.S.P.2015.000.31500.
- Lecompte, D., Smits, A., Sol, H., Vantomme, J. and Van Hemelrijck, D. (2007), "Mixed numerical-experimental technique for orthotropic parameter identification using biaxial tensile tests on cruciform

- specimens", *Int. J. Solid. Struct.*, **44**(5), 1643-1656. <https://doi.org/10.1016/j.ijsolstr.2006.06.050>.
- Lindner, D., Mathieu, F., Hild F., Alix, O., Minh, C.H. and Paulien-Camy, O. (2015), "On the evaluation of stress triaxiality fields in a notched titanium alloy sample via integrated digital image correlation", *J. Appl. Mech.-T.*, ASME, **82**(7), 1-10. <https://doi.org/10.1115/1.4030457>.
- Ludwik, P. (1909), *Elemente der Technologischen Mechanik*, Verlag von Julius Springer, Berlin, Germany.
- Martins, J.M.P., Andrade-Campos, A. and Thuilier, S. (2018), "Comparison of inverse identification strategies for constitutive mechanical models using full-field measurements", *Int. J. Mech. Sci.*, **145**, 330-345. <https://doi.org/10.1016/j.ijmecsci.2018.07.013>.
- Mathieu, F., Leclerc, H., Hild, F. and Roux, S. (2015), "Estimation of elastoplastic parameters via weighted FEMU and integrated-DIC", *Exp. Mech.*, **55**, 105-1129. <https://doi.org/10.1007/s11340-014-9888-9>.
- Nam Do, X., Ibrahimbegović, A. and Brancherie, D. (2015), "Combined hardening and localized failure with softening plasticity in dynamics", *Couple. Syst. Mech.*, **4**(2), 115-136. <https://doi.org/10.12989/csm.2015.4.2.115>.
- Neggiers, J., Mathieu, F., Hild, F., Roux, S. and Swiergiel, N. (2017), "Improving full-field identification using progressive model enrichments", *Int. J. Solid. Struct.*, **118**(7), 213-223. <https://doi.org/10.1016/j.ijsolstr.2017.03.013>.
- Passieux, J.C., Bugarin, F., David, C., Perie, J.N. and Robert, L. (2015), "Multiscale displacement field measurement using digital image correlation: Application to the identification of elastic properties", *Exp. Mech.*, **5**, 121-137. <https://doi.org/10.1007/s11340-014-9872-4>.
- Prates, P.A., Pereira, A.F.G., Oliveira, M.C. and Fernandes, J.V. (2019), "Analytical sensitivity matrix for the inverse identification of hardening parameters of metal sheets", *Eur. J. Mech. A Solid.*, **75**, 205-215. <https://doi.org/10.1016/j.euromechsol.2019.01.010>.
- Prates, P.A., Pereira, A.F.G., Sakharova, N.A., Oliveira, M.C. and Fernandes, J.V. (2016), "Inverse strategies for identifying the parameters of constitutive laws of metal sheets", *Adv. Mater. Sci. Eng.*, **2016**, 1-18. <https://doi.org/10.1155/2016/4152963>.
- Roux, S. and Hild, F. (2020), "Optimal procedure for the identification of constitutive parameters from experimentally measured displacement fields", *Int. J. Solid. Struct.*, **184**(2), 14-23. <https://doi.org/10.1016/j.ijsolstr.2018.11.008>.
- Sutton, M.A., Orteu, J.J. and Schreier, H.W. (2009), *Image Correlation for Shape, Motion and Deformation Measurements*, Springer, New York, USA.
- Tarantola, A. (1987), *Inverse Problems Theory. Methods for Data Fitting and Model Parameter Estimation*, Elsevier Applied Science, Southampton, UK.
- Tisza, M. (2005), "Numerical modeling and simulation in sheet metal forming academic and industrial perspectives", *Mater. Sci. Forum*, **473-474**, 407-414. <https://doi.org/10.4028/www.scientific.net/msf.473-474.407>.
- Tomičević, Z., Hild, F. and Roux, S. (2013), "Mechanics-aided digital image correlation", *J. Strain Anal. Eng. Des.*, **48**(5), 330-343. <https://doi.org/10.1177/0309324713482457>.
- Tomičević, Z., Kodvanj, J. and Hild, F. (2016a), "Characterization of the nonlinear behavior of nodular graphite cast iron via inverse identification: Analysis of uniaxial tests", *Eur. J. Mech. A Solid.*, **59**, 140-154. <https://doi.org/10.1016/j.euromechsol.2016.02.010>.
- Tomičević, Z., Kodvanj, J. and Hild, F. (2016b), "Characterization of the nonlinear behavior of nodular graphite cast iron via inverse identification: Analysis of biaxial tests", *Eur. J. Mech. A Solid.*, **59**, 195-209. <https://doi.org/10.1016/j.euromechsol.2016.02.010>.